

Materials Advances

Accepted Manuscript

This article can be cited before page numbers have been issued, to do this please use: A. S. Dayan, X. Zhong, M. Wierzbowska, C. E. M. Oliveira, A. Kahn and L. Etgar, *Mater. Adv.*, 2020, DOI: 10.1039/D0MA00452A.



This is an Accepted Manuscript, which has been through the Royal Society of Chemistry peer review process and has been accepted for publication.

Accepted Manuscripts are published online shortly after acceptance, before technical editing, formatting and proof reading. Using this free service, authors can make their results available to the community, in citable form, before we publish the edited article. We will replace this Accepted Manuscript with the edited and formatted Advance Article as soon as it is available.

You can find more information about Accepted Manuscripts in the [Information for Authors](#).

Please note that technical editing may introduce minor changes to the text and/or graphics, which may alter content. The journal's standard [Terms & Conditions](#) and the [Ethical guidelines](#) still apply. In no event shall the Royal Society of Chemistry be held responsible for any errors or omissions in this Accepted Manuscript or any consequences arising from the use of any information it contains.

The properties, photovoltaic performance and stability of Visible to Near-IR all inorganic perovskite

View Article Online

DOI: 10.1039/D0MA00452A

Adva Shpatz Dayan¹, Xinjue Zhong², Malgorzata Wierzbowska³, C. E. M. de Oliveira⁴, Antoine Kahn², Lioz Etgar^{1,*}

¹ Institute of Chemistry, Casali Center for Applied Chemistry, The Hebrew University of Jerusalem, Jerusalem 91904, Israel.

²Department of Electrical Engineering, Princeton University, Princeton, New Jersey 08544, USA

³Institute of High Pressure Physics, Polish Academy of Sciences Sokołowska 29/37, 01-142 Warsaw, Poland

⁴The Center for Nanoscience and Nanotechnology, The Hebrew University of Jerusalem, Jerusalem 91904, Israel

* lioz.etgar@mail.huji.ac.il

Keywords: Inorganic perovskite, Near-IR, stability, hall mobility, CsPbI₃

Hybrid metal halide perovskites have seen an exponential increase in the scientific community due to their successful introduction in solar cells. However these materials are known to suffer from thermal instability, toxicity and limited absorption range. One way to overcome these obstacles is by substituting the organic cation with an inorganic one and by replacing the lead by tin, which can shift the absorbance to the near infrared (NIR). In this work we synthesized several compositions of all inorganic CsSn_yPb_{1-y}Br_xI_{3-x} (0 < y < 1, 0 < x < 3) perovskites achieving a wide band gap range from 1.3 eV to 1.75 eV. It was found that Sn stabilizes the CsPbI₃ black photovoltaic (PV) active phase and at the same time shifts the absorbance to the NIR. Although some of these perovskite compositions are already known, here we analyzed in detailed their physical and electronic properties. Hall effect measurements show an increase in the carrier concentration and hall mobility with the addition of Sn. Interestingly the hall mobility is five times higher for CsSnI₃ than in the case of having just 10% Pb and 90% Sn in



the perovskite structure. Ultraviolet photoemission spectroscopy (UPS) and Density functional theory (DFT) calculations reveal the energy level position and a phase mixing, which explain the reduction in the photovoltaic performance with the addition of Sn. The best PV performance of 12.7% efficiency was achieved in the case of 80:20, Pb:Sn ratio, which is one of the highest PCE reported for similar perovskite compositions.

1. Introduction

Organic–inorganic perovskites are being used today in a variety of optoelectronic applications. Hybrid perovskites have several unique properties, which makes them attractive semiconductors for use in the photovoltaic (PV) field.¹⁻³ In order for the perovskite to function efficiently as a light harvester in the solar cell, it must be stable under environmental conditions (especially moisture)⁴⁻⁶ and have high photostability for long term use.⁷⁻⁹

The general formula of basic halide perovskites is ABX_3 where A is generally an organic cation (Methylammonium- MA^+ , Formamidinium - FA^+) but can be also an inorganic cation (Cs^+); B is a divalent metal cation (Pb^{2+} , Sn^{2+} , Ge^{2+} , Sr^{+2} , and Cu^{+2})¹⁰⁻¹³ and X is a halide anion (Cl^- , Br^- , I^-).

The common hybrid perovskite used in solar cells over the past few years is $CH_3NH_3PbI_3$ ($MAPbI_3$). However, this material has an organic cation (usually MA^+) which makes the entire structure relatively unstable under high temperature.¹⁴⁻¹⁶ Moreover, the use of Pb as the divalent cation is problematic due to its toxicity.¹⁷⁻¹⁹ Several reports show that the replacement of the organic cation by an inorganic cation can improve the stability of the perovskite.²⁰⁻²⁶ Following this direction, one of the potential candidates is $CsPbI_3$ which has an absorbance onset around 700 nm. $CsPbI_3$ has four phases: α, β, γ and δ but only α and β can be used in PV solar cells while γ and δ are metastable phases that are inactive in PV cells.²⁷ The transition between the phases usually happens due to exposure to air when the α phase, which is cubic, transforms to the β phase (tetragonal structure) and then to the γ and δ phases (orthorhombic structure). In our previous report, we showed that $CsPbI_3$ can be stabilized in two dimensional structure (2D),²⁸ however it forms a wide band gap which makes it problematic to function efficiently in a solar cell.²⁹ Other methods to stabilize



the CsPbI₃ active phase include the addition of different salts such as EuBr₂, EuCl₂ and CaI₂.²⁵⁻³¹

Modifying the B site in CsPbI₃ can tune the optical properties and at the same time can enhance its stability. The replacement of lead (Pb) by tin (Sn) in the case of MA⁺ based perovskites leads to a variation in the band gap from 1.55 eV for MAPbI₃ to 1.3 eV for MASnI₃.³²⁻³⁵ Replacing the Pb by Sn in the case of full inorganic perovskite (Cs based perovskite) might assist to get a stable structure and at the same time will shift the absorbance to the near-IR. Moreover, introducing Sn instead of the Pb will reduce toxicity the of the perovskite.

In order for another element to be able to replace Pb²⁺ in the perovskite structure, it needs to have a coordination number equal to six and a similar ionic radius. Additional indication can be obtained from the Goldschmidt tolerance factor (**Equation 1**), where r_A is the radius of the A cation, r_B is the radius of the B cation, and r_X is the radius of the anion.

$$t = \frac{r_A + r_X}{\sqrt{2}(r_B + r_X)} \quad (1)$$

The ionic radius of Sn²⁺³⁶ is smaller than that of Pb²⁺³⁶, therefore when introducing more Sn²⁺ instead of Pb²⁺, the tolerance factor increases and as a result we observe a perovskite which has a stable structure compared to CsPbI₃.³⁷⁻³⁸ In addition, the Sn-I bond length is shorter than the Pb-I bond length, which supports a stable structure in the case of Sn-based perovskites.

The radius of the inorganic cation (Cs⁺) is smaller than that of the MA⁺, which suggest further enhancement in the stability of the structure.³⁹ CsSnI₃ was demonstrated first in 2012 by Chung et al.,⁴⁰ who used it as hole transport material (HTM) in dye-synthesized solar cells.⁴¹ In 2016 Wang et al. studied CsSnI₃ as the light harvester material in a solar cell and reported an efficiency of 3.31%.⁴² The combination of Sn and Pb in the solar cell was reported using organic cations (MA⁺ and FA⁺), achieving a power conversion efficiency (PCE) of 15%. In addition, in 2015 Sabba et al. published their work using CsSnI_{2.9}Br_{0.1} as light harvester material in a solar cell and achieved a low PCE of 1.67%.⁴⁰ Other reports demonstrate the use of bromide and mixed halides with solely Sn in the solar cells.⁴³⁻⁴⁵

Liu et al. synthesized CsSn_{1-x}Pb_xI₃ and CsSn_{1-x}Pb_xBr₂I nanocrystals and used them in light emitting diode devices.⁴⁶ In 2017 Liang et al. used all inorganic perovskite with mixed halides (Br, I).⁴⁷ In this study they used CsPbBr₃, CsPbIBr₂ and a specific



composition $\text{CsPb}_{0.9}\text{Sn}_{0.1}\text{I}\text{Br}_2$ (where the amount of Sn is no more than 10%), and demonstrated a PCE of 11.33%. A year later Li et al. used $\text{CsPb}_{0.75}\text{Sn}_{0.25}\text{I}\text{Br}_2$ perovskite (keeping the ratio between the halides constant), achieving slightly higher PCE of 11.53%.⁴⁸

Although these compositions were already discussed in the literature, here we shed light on their physical, stability and electronic properties using hall effect measurement and ultraviolet photoelectron spectroscopy (UPS). We combine inorganic cation (i.e. Cs^+) with Pb and Sn at the B site of the perovskite. We synthesize and study materials using various ratios of Sn and Pb based on the chemical formula $\text{CsSn}_y\text{Pb}_{1-y}\text{Br}_x\text{I}_{3-x}$ (**Table 1**). As a result we were able to achieve a wide range of band gaps from 1.3 eV to 1.75 eV. The Hall effect and UPS measurements reveal the hole mobility, carrier density and the energy levels position of this full inorganic perovskite. The stability under humidity and photostability of these compositions as films and full devices are also studied. Finally, we demonstrate the application of these compositions into mesoporous perovskite based solar cells, achieving one of the highest efficiencies reported for $\text{CsSn}_y\text{Pb}_{1-y}\text{Br}_x\text{I}_{3-x}$ perovskites.

Table 1: Perovskite compositions studied in this work, $\text{CsSn}_y\text{Pb}_{1-y}\text{Br}_x\text{I}_{3-x}$ ($0 < y < 1$, $0 < x < 3$)

Pb:Sn ratio	Perovskite composition
100:0	CsPbI_3
90:10	$\text{CsSn}_{0.1}\text{Pb}_{0.9}\text{I}_{2.8}\text{Br}_{0.2}$
80:20	$\text{CsSn}_{0.2}\text{Pb}_{0.8}\text{I}_{2.6}\text{Br}_{0.4}$
70:30	$\text{CsSn}_{0.3}\text{Pb}_{0.7}\text{I}_{2.4}\text{Br}_{0.6}$
60:40	$\text{CsSn}_{0.4}\text{Pb}_{0.6}\text{I}_{2.2}\text{Br}_{0.8}$
50:50	$\text{CsSn}_{0.5}\text{Pb}_{0.5}\text{I}_2\text{Br}_1$
40:60	$\text{CsSn}_{0.6}\text{Pb}_{0.4}\text{I}_{1.8}\text{Br}_{1.2}$
30:70	$\text{CsSn}_{0.7}\text{Pb}_{0.3}\text{I}_{1.6}\text{Br}_{1.4}$
20:80	$\text{CsSn}_{0.8}\text{Pb}_{0.2}\text{I}_{1.4}\text{Br}_{1.6}$
10:90	$\text{CsSn}_{0.9}\text{Pb}_{0.1}\text{I}_{1.2}\text{Br}_{1.8}$
0:100	CsSnI_3



2. Results and discussion

Introducing Sn (instead of Pb) into the perovskite structure can lead to four different phases, as in the case of CsPbI₃, with some of them being PV active. Since Cs⁺ is used as the cation, it occupies the 1b Wyckoff position in the center of the perovskite cube, and therefore it is easier to create the ideal cubic $Pm\bar{3}m$ structure than in the case of most of the organic cations.

Our motivation here was to find a way to stabilize the active CsPbI₃ phase. Here we used the Sn²⁺ cation in addition to the Pb²⁺ cation in order to create a good overlap between the orbitals of the divalent metal cation (Pb²⁺ and Sn²⁺) and the orbitals of the halide anion (I⁻, Br⁻). The band gap of these semiconductors is determined by the orbitals of the halide and the divalent metal cation.⁴⁹ It is known that the valence-band maximum (VBM) is predominantly determined by the anti-bonding component of the hybridization between the divalent metal in B site and the halide in the X site, while the conduction-band minimum (CBM) is dominated by the nonbonding component of the divalent metal. In the case of Pb halides, the overlap of Pb-I/Br is between the 6s orbital of Pb²⁺ and the 5p or 4p orbitals of I⁻ or Br⁻, respectively. The 6s and 6p orbitals of Pb are at higher binding energy compared to the 5s and 5p orbitals of the Sn, as a result the binding energy of the s-p hybridized antibonding levels are lower for Sn (5s) and (5p) - X(p) than for Pb(6s) and (6p) - X(p). As a consequence, both the VBM and CBM undergo an upshift when Sn replaces Pb.⁵⁰

Figure 1 a-b show the absorbance as a function of Sn concentration in CsSn_yPb_{1-y}Br_xI_{3-x} perovskite structure. The absorption edge shifts to longer wavelength and extends to the Near Infra-Red (NIR) region with increasing Sn concentration. Similar bandgap changes have been observed in MASn_xPb_{1-x}I₃.³²

In order to compare the influence of the B site (i.e. Sn Vs. Pb) to that of the X site (i.e. I vs. Br) on the optical properties, we synthesized CsSn_yPb_{1-y}I₃ and CsSn_yPb_{1-y}Br_xI_{3-x}, (0 < y < 1, 0 < x < 3). In the synthesis of CsSn_yPb_{1-y}Br_xI_{3-x} the bromide has one source, i.e., SnBr₂, whereas the iodide has two sources, PbI₂ and CsI.



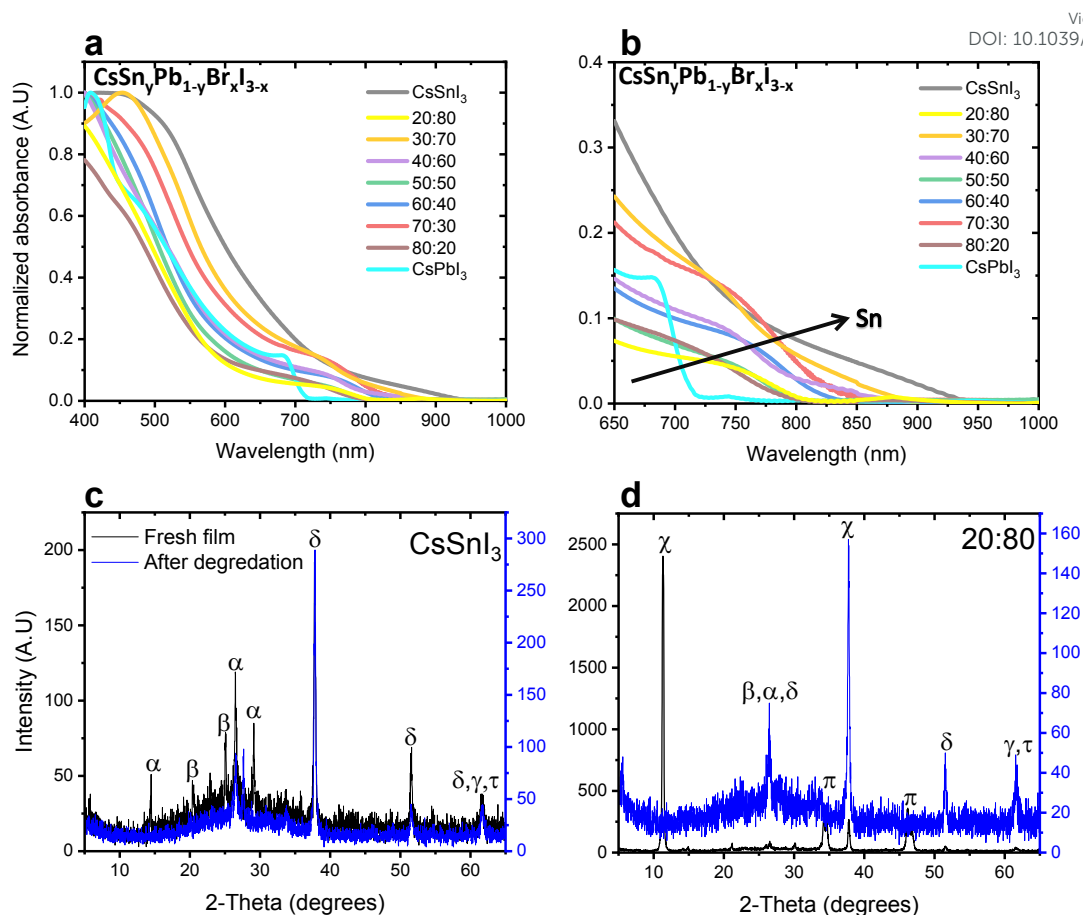


Figure 1. a) Absorbance spectra of $\text{CsSn}_y\text{Pb}_{1-y}\text{Br}_x\text{I}_{3-x}$ ($0 < y < 1$, $0 < x < 3$) films encapsulated at different ratios of Pb:Sn. (b) Magnification of the absorbance spectra (shown in 1a) in the range of 650-1000 nm. XRD patterns of c) CsSnI_3 and d) $\text{CsSn}_{0.8}\text{Pb}_{0.2}\text{I}_{1.4}\text{Br}_{1.6}$ (Pb:Sn-20:80) before and after degradation. (π - CsPbI_3 cubic phase, χ - CsPbI_3 orthorhombic phase, α - CsSnI_3 , δ - SnO_2 , β - SnI_2 , γ - PbI_2 , τ - CsI).

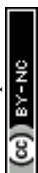
Figure 2a shows the band gap as a function of the Pb:Sn ratios in both cases mixed bromide-iodide and pure iodide. As was discussed above the band gap decreases with the addition of Sn. Moreover, the influence of the bromide on the band gap is also observed. The change in the band gap is more pronounced in the case of pure iodide compare to the case of mixed iodide-bromide. The bromide shifts the absorbance to shorter wavelength which compensate slightly on the red shift due to the addition of Sn. This can be explained when looking on the slope of the curves in **Figure 2a**. The slope of the green dots (pure iodide) is larger by 1.5 times than the slope of the blue dots (mixed bromide-iodide). All the absorbance spectra can be seen in **Figures S1 and S3**. Therefore, we can suggest that the influence of the Sn on the band gap is more



pronounced than the bromide in this case. We were able to achieve a wide range of band gaps from 1.3 eV to 1.75 eV.

X-ray diffraction (XRD) measurements were performed for different ratios of Pb:Sn. Figure 1c-d show the cases of pure CsSnI₃ and CsSn_yPb_{1-y}Br_xI_{3-x} with a 20:80 Pb:Sn ratio, respectively. (Other Pb:Sn ratios are presented in the supporting information in Figure S2). The black curve corresponds to the fresh film while the blue curve corresponds to the film after degradation. In our previous work we found that after 48 hours at room conditions (ambient air) a full degradation is observed.²⁸ We determine full degradation of the perovskite by absorbance and XRD measurements, which indicate the presence of the material's precursors (mainly PbI₂ and CsI). Figure 1c exhibits peaks related to CsSnI₃, ($2\theta = 14, 27, 29$) and SnI₂ ($2\theta = 22, 28$), where peaks related to SnO₂ ($2\theta = 39, 62$) can be observed just after degradation due to the Sn oxidation. The spectrum for 20:80 Pb:Sn ratio can be seen in Figure 1d, where the cubic and the orthorhombic phases of CsPbI₃ can be observed. After degradation, the perovskite dissociates into SnI₂, PbI₂ and CsI. The presence of CsPbI₃ in the fresh film suggests that both CsPbI₃ and CsSnI₃ are formed.

The photostability measurements on the synthesized hybrid CsSn_yPb_{1-y}Br_xI_{3-x} and CsSn_yPb_{1-y}I₃ were performed under continuous 1 sun illumination, 18 °C and 27% humidity. Figure 2b summarizes these measurements for different Pb:Sn ratios. For each ratio we followed the absorbance spectra as a function of time. The corresponding absorbance spectra are presented in Figure S4 and S5. It can be seen clearly that as the Sn amount increases, the photostability of the perovskite increases. For example, at Pb:Sn ratio of 20:80, the perovskite does not degrade for 172 hours under continuous 1 sun illumination, 18 °C and 27% humidity. Interestingly, even in the case of 20% Sn in the perovskite structure, the photostability improved notably compare to pure CsPbI₃. An important observation from these measurements is that the mixed halide (iodide and bromide) perovskite is more photostable than the single halide (i.e. iodide) perovskite in the structure. Based on this fact, the rest of the work have been concentrated on the mixed halide perovskite. Scanning electron microscopy (SEM) micrographs of the films before and after degradation (48 hours) are presented in Figure S6. After degradation there are more pinholes and the grain boundaries are better defined than in the case of fresh films.



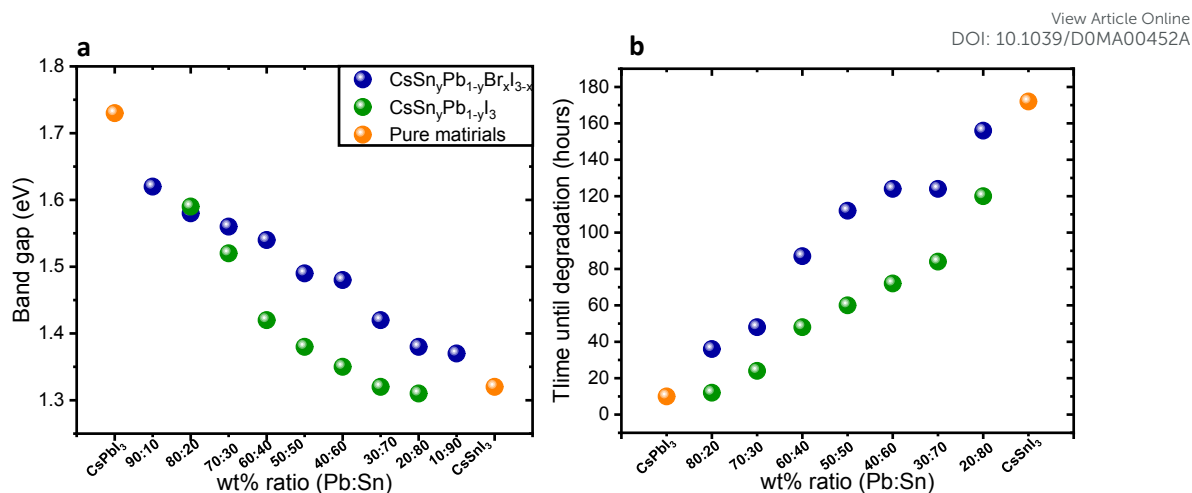


Figure 2. a) The band gap as a function of the Pb:Sn ratio for the cases of mixed iodide and bromide and for pure iodide compounds. The slope of the green dots is 1.5 times larger than the slope of the blue dots. b) Photostability measurements under 1 sun illumination, 18°C and 27% humidity. The data in this graph are based on the absorbance spectra shown in Figure S4 and S5.

Following the photostability measurements, we explored the stability of the different samples under room conditions and without encapsulation. The photographs of the films as a function of time are shown in Figure S7 and S8. Similar to the case of the photostability measurements, when the ratio of Sn : Pb is higher, the perovskite is more stable in air without encapsulation. It can be seen that CsSnI₃ is stable in air for over 48 hours. Similar to the photostability measurements, films with Pb:Sn ratios of 20:80, 30:70 and 40:60 showed excellent stability for over 24 hours. It is important to keep in mind that CsPbI₃ cannot survive more than 10 min in air.²⁸ These experiments (photostability and stability) indicate clearly that the resistance of the perovskite to humidity is enhanced when the Pb is replaced by Sn. This enhanced stability is in contrast to the case of perovskite with mixed Pb and Sn having an organic cation at the A site. In this case the stability decreases by more than 50% when introducing Sn into the perovskite.⁵¹ In our case (see figure 3), since Cs is used as the inorganic cation at the A site, the lattice parameter is reduced and the cubic structure shrinks compared to the case of an organic cation which change the tolerance factor, this slows down the oxidation reaction of the Sn and provides enhanced stability.⁵¹ In addition to that effect, it was found that mixed halide perovskites (iodide and bromide) have better stability than single halide (iodide) perovskites.⁵²



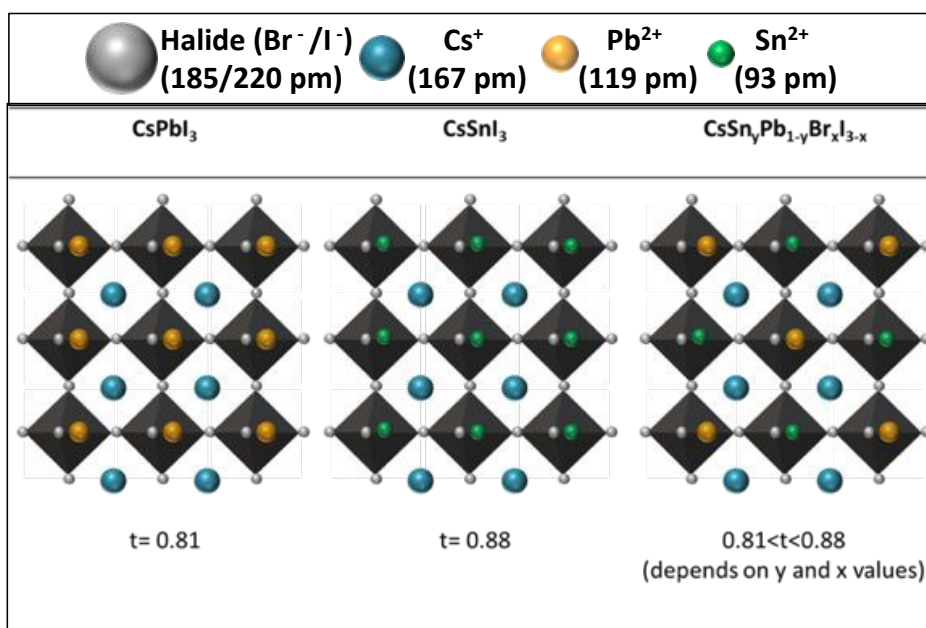
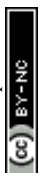


Figure 3. Schematic illustration of the change in the tolerance factor as a result of Cs, Pb and Sn in the perovskite structure.

In order to study the hole mobility, carrier concentration and resistivity for the various Pb:Sn ratios, Hall effect measurements were performed. When a magnetic field is applied on a conductor or a semiconductor that carries an electric current, a potential difference across the sample and perpendicular to both the current and the magnetic field will be developed. This is called the Hall effect, and the potential difference developed across the sample is the Hall voltage (V_H). By measuring the Hall voltage, it is possible to get the nq product, the mobile carrier density multiplied by the charge carrier. (n –electron density, q - charge of carrier). Several studies showed the use of hole effect measurements to reveal the properties of 2D materials such as black phosphorene.^{53,54}

Hall effect measurements were performed on perovskite films deposited on microscope glass substrates with four gold contacts at the corners. It can be observed in **Figure 4a-c** that, as the amount of Sn increases, the carrier concentration and the mobility increase, while the resistivity decreases. This trend can be explained by the oxidation of the Sn. It is known that Sn^{2+} oxidizes easily in ambient atmosphere to Sn^{4+} .⁵¹ The replacement of Sn^{2+} by Sn^{4+} in the perovskite structure has been linked to hole doping, which increases the number of carriers⁵⁵ and can explain the decrease in resistivity as shown in **Figure 4a**. As the Pb:Sn ratio increases, there is more Sn in the structure, which



potentially can be oxidized, and **Figure 4** shows that the carrier concentration, hole mobility and resistivity change as a function of this ratio.

The carrier type determines the semiconductor type. The Hall effect measurement can assist to determine the type of these semiconductors. It was observed that with the addition of Pb into the perovskite structure the behavior of the film is becoming less p-type. In general, when doping the structure with Pb influences dramatically the properties (mobility, carrier concentration and resistivity) compare to perovskite which is solely based on Sn.

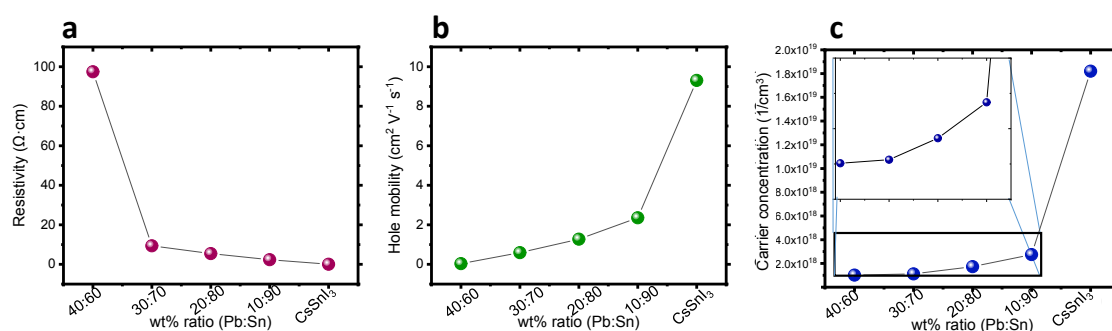


Figure 4. Hall effect measurement of the different ratios Pb:Sn: a) Resistivity, b) Hole mobility, c) Carrier concentration.

Energy levels of films with different ratios of Pb:Sn were measured by ultraviolet photoemission spectroscopy (UPS). The perovskite films were spin-coated on conductive indium tin oxide (ITO)/glass substrates. **Figure 5a-b** show the photoemission cut-off and the VBM, respectively, measured on CsSn_{0.2}Pb_{0.8}I_{2.6}Br_{0.4}. The cut-off position yields a work function of 4.77 eV. The valence band spectrum, recorded and plotted on a logarithmic scale, shows the VBM at 0.89 eV below the Fermi level (0 eV on the energy scale). The ionization energy (IE) of this film (Pb:Sn - 80:20) is therefore 5.66 eV. Measurements on films with various Pb:Sn ratios show that IE decreases to 5.64 eV for 70:30, 5.56 eV for 60:40, and finally to 5.37 eV for 20:80 (see Figure S9). By combining the optical bandgap and the VBM position, the position of the CBM can be estimated, assuming that the exciton binding energy is small and negligible with respect to the photoemission resolution in 3D perovskites.⁵⁶⁻⁵⁸ The CBM shifts to higher energy with increasing Sn²⁺ concentration, following the trend of the VBM, as shown in **Figure 5c**. The IE of CsPbI₃ is higher than expected mainly due to the fast degradation of the film during sample transfer. It has been reported^{59,50} that VBM arises from antibonding hybridization of Pb (6s) and/or Sn (5s) and halide (np)



orbitals. The lower binding energy of the Sn 5s orbitals compared to the Pb 6s orbitals upshifts the VBM with increasing Sn content, which is consistent with the experimental results. The CBM is derived from the hybridization of the antibonding Pb (6p) and/or Sn (5p) state and the halide (np) orbitals with major contribution from Pb (6p) and/or Sn (5p). Some reports suggest that the CBM of the Pb-Sn alloy is mainly composed of Pb 6p and I 5p orbitals since the binding energy of the Sn 5p orbital is lower than that of the Pb 5p orbital.⁶⁰ The addition of Sn and Br in the mixed perovskites reduces the lattice constant and thus enhances the hybridization, which pushes the CBM to higher energy.⁶¹ **Figure 5d** shows the experimental and calculated band gaps for the different ratios. Density functional theory (DFT) was used for the band gap calculations (see more details in the experimental section). The experimental band gaps are in between the calculated band gaps for the cubic structure and the orthorhombic structure. It can be suggested that our different films have a mix of cubic and orthorhombic structures. For low amount of Sn, the cubic structure is dominant, but when the Sn amount increases the orthorhombic structure (which is a metastable phase) starts to appear. Since the orthorhombic structure is inactive in solar cells, it influences the PV results as is discussed below.

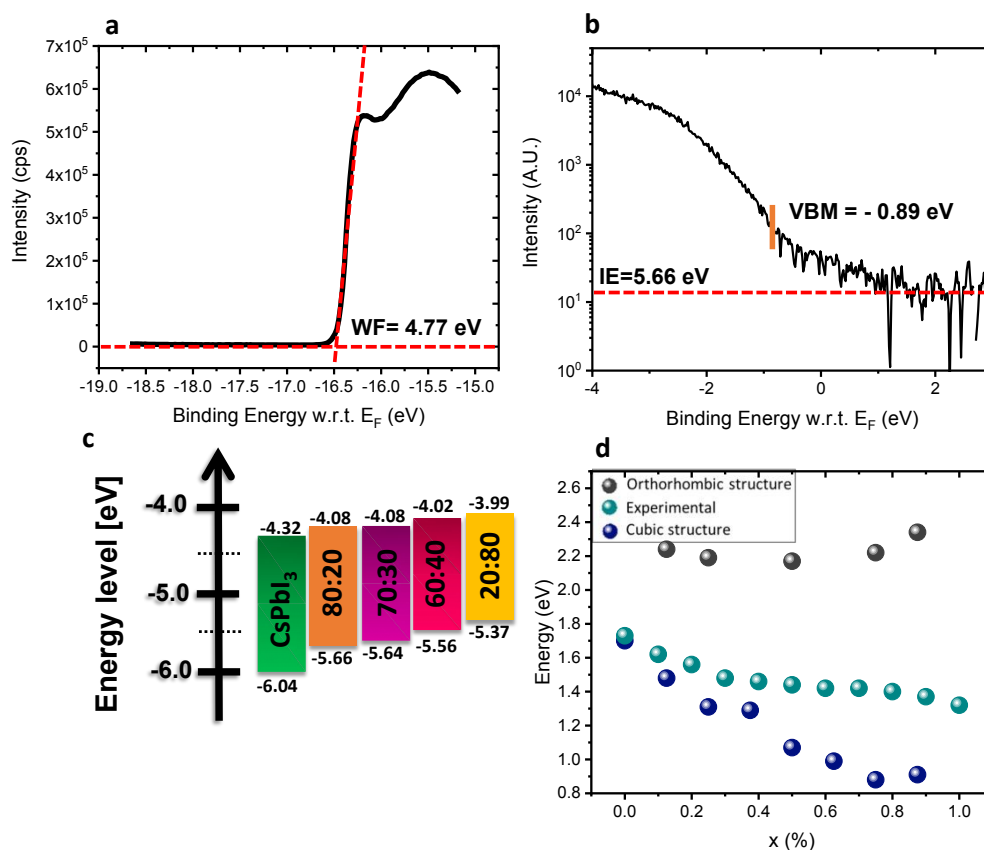


Figure 5. a) Photoemission cut-off measured via UPS for $\text{CsSn}_{0.2}\text{Pb}_{0.8}\text{I}_{2.6}\text{Br}_{0.4}$. b) The position of the VBM and ionization energy (IE) for $\text{CsSn}_{0.2}\text{Pb}_{0.8}\text{I}_{2.6}\text{Br}_{0.4}$ measured by UPS. c) Energy diagram of the different materials used in this study. The band gap of CsPbI_3 is relatively wide with respect to the literature value,⁶² which is due to degradation as discussed in the text. d) Experimental results and theoretical calculation of the band gaps for the various ratios when adding SnBr_2 . X represents the ratio Pb:Sn.

View Article Online
DOI: 10.1039/D0MA00452A

Based on our chemical and physical characterizations, we introduced several perovskites with different ratios of Pb:Sn into solar cells. We investigated three ratios of Pb:Sn - 80:20, 70:30 and 60:40 using PTAA (Poly[bis(4-phenyl)(2,4,6-trimethylphenyl)amine] as the hole transport material, as presented in **Figure 6b**. **Figure 6a** shows an SEM cross section of the discussed solar cell, where the different layers can be observed clearly.

The solar cell structure is based on mesoporous TiO_2 , on which the Cs-based perovskite is deposited. To our knowledge, there is to date no report on the black phase of CsPbI_3 on mesoporous layer. Most reports show the black CsPbI_3 perovskite phase in the planar configuration (compact TiO_2 or PEDOT:PSS).^{63,64}

The HOMO and LUMO levels of PTAA are shown in the supporting information (Figure S10). As the Pb amount is larger, the PV performance is better, except for the pure CsPbI_3 which is highly unstable (**Table 2**). The experimental and calculated band gaps show that as the Sn concentration increases inside the perovskite, the orthorhombic structure becomes dominant. This phase is inactive for PV solar cells and therefore reduces the PV parameters. The 60:40 ratio of Pb:Sn gives the worst PV performance. This is the result of the orthorhombic structure but is also due to two structures formed in this case, the CsPbI_3 and the CsSnI_3 perovskites. Therefore, the physical and electronic properties are not the optimal to function as an efficient light harvester in the solar cell. On the other hand, in the case of 80:20 Pb:Sn ratio the PV performance was the highest achieving 12.7% power conversion efficiency (see **Figure 6c** and **Table 2**), which is one of the highest PCE reported for similar perovskite compositions. Forward and reverse scans of the IV curve (Figure S11) show minimal hysteresis for these cells.



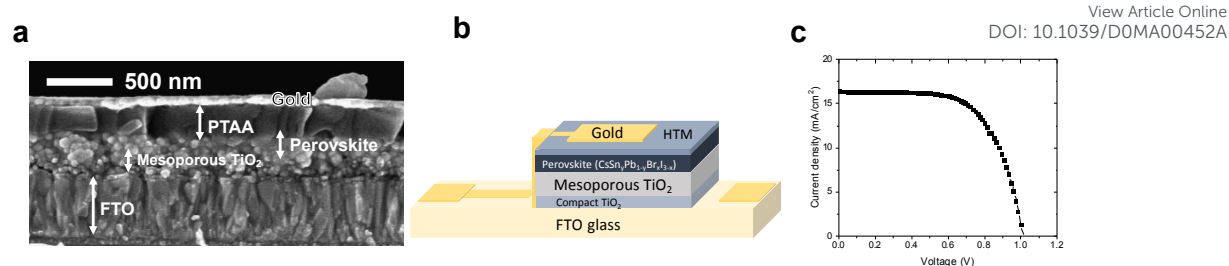
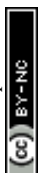


Figure 6. a) Cross section SEM image of the PSC with ratio of 80:20 ($\text{CsSn}_{0.2}\text{Pb}_{0.8}\text{I}_{2.6}\text{Br}_{0.4}$) (Pb:Sn) and PTAA as the HTM. b) Schematic illustration of the perovskite solar cell configuration used in this work. (c) JV curve of the champion cell presenting 12.7% efficiency, FF of 64.2%, J_{sc} of 19.09 mA/cm^2 and V_{oc} of 1V.

Table 2. Best PV parameters and average PV parameters (in brackets) for different ratios of Pb:Sn. Average of 20 cells.

Pb:Sn ratio	V_{oc} [V]	J_{sc} [mA cm^{-2}]	Fill factor [%]	PCE [%]
80:20	1.00 (0.95 ± 0.03)	19.09 (18.71 ± 0.47)	64.27 (62 ± 1.47)	12.70 (10.10 ± 0.23)
70:30	0.84 (0.83 ± 0.01)	13.84 (13.01 ± 0.12)	44.25 (43.17 ± 1.02)	4.60 (4.11 ± 0.24)
60:40	0.78 (0.77 ± 0.04)	7.49 (6.85 ± 1.47)	41.44 (39.58 ± 1.47)	2.79 (2.01 ± 0.02)

The stability of the full solar cells was studied under different conditions, as presented in **Figure 7a and 7b**. The stability measurements presented in **Figure 7a** were performed under continuous 1 sun illumination (the corresponding other PV parameters of these cells are presented in Figure S12 a-c). An increase in the PV performance can be observed in the first 4 to 10 hours of continuous illumination for all Pb:Sn ratios. Following that, the PV performance of the cells decreases in all cases. Table S1 shows the change in the PV parameters, before illumination and after reaching the highest PV performance. The change in the PV parameters is the largest for the 80:20 ratio. Introducing more Sn into the perovskite leads to smaller changes in the PV parameters during continuous illumination. The increase of the PV parameters upon continuous



illumination shows the sensitivity of those perovskite compositions to light, as also discussed along this work. **Figures 7b** and S12 d-f show the stability of the cells stored under inert atmosphere, where the J-V curves were measured in air. In the beginning (45-50 hours) there is a drop in the PV performance for all ratios. Thereafter, the PV performance remains stable for 400 hours. To summarize, the complete solar cells degraded under continuous illumination (after an initial increase), similar to the photostability of the films with the same composition (same Pb:Sn ratios) as presented in Figure 2b. Still the full cells are slightly less stable than the films, which is probably due to the additional HTM and the measurement conditions.

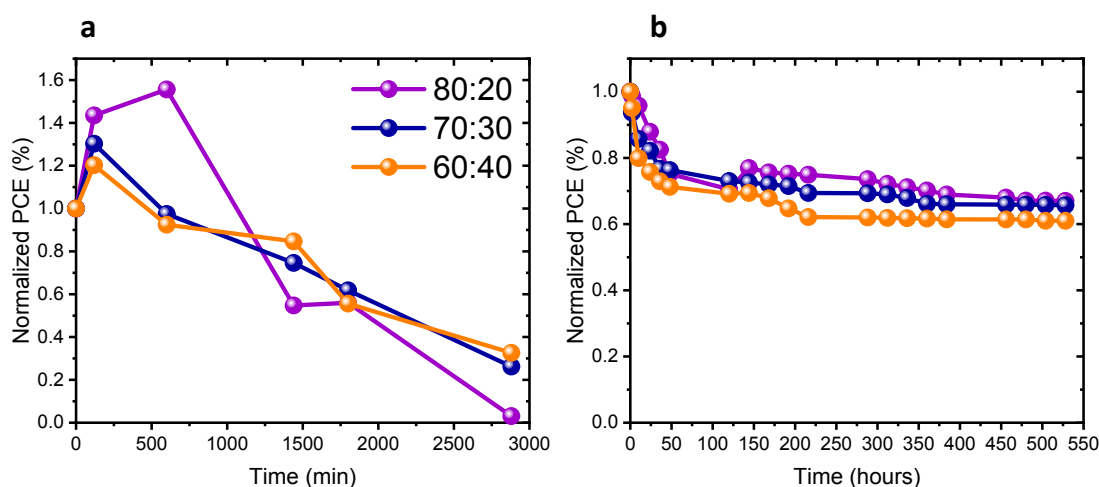


Figure 7. (a) Stability under 1 sun illumination of complete solar cells with different ratios of Pb:Sn as discussed in this work. (b) Stability of the cells stored under inert atmosphere and measured in the open air with encapsulation.

3. Conclusion

In this work $\text{CsSn}_y\text{Pb}_{1-y}\text{Br}_x\text{I}_{3-x}$ all inorganic perovskites were synthesized at various ratios of Pb:Sn. Stability and photostability measurements show that the Sn stabilizes the CsPbI_3 black PV active phase. The Cs cation shrinks the cubic structure and as a result slows down the oxidation of the Sn. The Hall effect measurement shows an increase in the mobility and in the charge carrier density with the addition of Sn to the structure. UPS reveals an upward shift of the VBM and a small increase in the CBM which provide a decrease in the band gaps with the increase of the Sn amount in the structure. Finally, these compounds were introduced into mesoporous based perovskite solar cell achieving 12.7% power conversion efficiency. As the Sn amount increase the



PV performance decrease due to phase mixing of the active cubic phase and the nonactive orthorhombic phase supported by DFT calculations. View Article Online
DOI: 10.1039/D0MA00452A

4. Experimental Section

Films fabrication: Microscope glass was cleaned with ethanol and acetone. Oxygen plasma treatment (80% power, diener) before deposition of the perovskite solution.

Device fabrication: SnO₂/ (FTO) conductive glass (10 O cm¹, Pilkington) was etched by the reaction of zinc powder with HCl (37% Sigma) on top of the glass. After etching the glass was cleaned in sonication bath for 15 minutes following oxygen plasma treatment (80% power, diener). The compact TiO₂ (TiDIP, 75% in isopropanol Aldrich diluted 1:5 in isopropanol) layer was deposited on the substrate by spin coating (5000 rpm for 30 seconds), followed by deposition of m-TiO₂ nanoparticles (30-NRD, dyesol) (1.6 w/w% in ethanol absolute) spin-coated (5000 rpm for 30 seconds); then the substrate was annealed to 450 °C for 30 min. TiCl₄ was applied on the m-TiO₂ film.

For the perovskite deposition, 60 μL of perovskite solution was dropped on the middle of the substrate, followed by a spin-coated process with five seconds delay time, ten seconds spin at 1000 rpm, and 45 seconds spin at 5000 rpm. 25 seconds before the end of the spin coating, 50 μL of toluene were added dropwise onto the substrate. The cells were annealed at 110 °C for two minutes. Next, the PTAA film was deposited: A PTAA (Ossila)/toluene (15 mg/1 ml) solution with added 13.6 ml of Li-bis(trifluoromethanesulfonyl) imide (Li-TFSI)/acetonitrile (28.3 mg/1 ml) and 6.8 ml TBP was spin-coated at 3000 rpm for 30 seconds and annealed at 75 °C for five minutes. Finally, a 70 nm thick gold electrode was thermally evaporated on the film under a vacuum of ~10⁻⁷ Torr.

Preparation of Perovskite Solutions: The perovskite solutions were prepared in a nitrogen filled glovebox H₂O < 0.1 ppm and O₂ < 5.0 ppm. All of the inorganic precursors were purchased from Sigma Aldrich. The solution of CsSn_yPb_{1-y}Br_xI_{3-x} (different ratios) solution of 0.48 M was prepared by dissolving CsI, PbI₂, SnBr₂, in a mixture of dimethylformamide: dimethyl sulfoxide (DMF/DMSO) (85%:15%). A CsSnI₃ solution (0.48 M) was prepared by dissolving CsI, PbI₂, SnI₂, in a mixture of dimethylformamide: dimethyl sulfoxide (DMF/DMSO) (85%:15%). The perovskite solutions were prepared 12 hours before the perovskite deposition.

Encapsulation: Encapsulation was done with Meltonix 1170-60 (Solaronix) and cover glasses (PAUL MARIENFELD) at nitrogen environment.



Absorbance Measurements: Absorbance measurements were performed using a Jasco V-670 spectrophotometer. View Article Online
DOI: 10.1039/D0MA00452A

X-ray Diffraction (XRD): X-ray powder diffraction measurements were performed in grazing incidence X-ray diffraction (GIXRD) mode on the D-8 advance diffractometer (Bruker AXS, Karlsruhe, Germany) with a goniometer radius of 217.5 mm. A secondary graphite monochromator, 2° Soller slits and a 0.2 mm receiving slit. XRD patterns within the range 2° to 60° (2 θ) were taken at 273 K using CuK α radiation (1 $\frac{1}{4}$ 1.5418 °Å) with the following measurement conditions: tube voltage of 40 kV, tube current of 40 mA, step-scan mode with a step size of 0.02° (2 θ) and counting time of 1 s⁻³ s per step. The value of the grazing incidence angle was 2.5°.

Ultra High Resolution Scanning Electron Microscopy (UHR-SEM): The images attained by using Sirion UHR SEM of FEI (Field Emission Instruments). The measurement conditions were 5 kV, the spot size was 3.0, the detector was TLS.

Hall Effect: Hall Effect measurements were obtained using Lake Shore dc Hall effect system model 8404. A magnetic field of 1.7 T, and a current of 100 nA were used in the measurement. The samples were illuminated by 0.25 sun of white LED source. Each measurement was conducted 20 times, the average results and the standard deviations were used to the calculation of the final values. Also, in these measurements we used the high resistivity option in order to achieve reliable results.

Ultraviolet photoelectron spectroscopy (UPS) : UPS measurements were performed in ultrahigh vacuum at room temperature. He I photons (21.22 eV) generated by a discharged lamp were used to probe the work function and valence band edges.

Photovoltaic Characterization: Photovoltaic measurements were using a New Port system, composed of an Oriel I–V test station using an Oriel Sol3A simulator. The solar simulator is class AAA for spectral performance, uniformity of irradiance, and temporal stability. The solar simulator is equipped with a 450 W xenon lamp. The output power is adjusted to match AM1. The spectral matched classic cations are IEC60904-9 2007, JIC C 8912, and ASTM E927-05.

DFT calculations: The density functional theory (DFT) calculations of the band gaps were performed with the Quantum ESPRESSO code ⁶⁵, using the plane-wave basis and norm-conserving pseudopotentials for the atomic cores. The Perdew-Burke-Ernzerhof parametrization of the exchange-correlation functional was chosen. The spin-orbit coupling was not included, because its effect on the bandgaps in perovskites is balanced by a neglect of the self-interaction correction (see Table 5 in Ref. ⁶⁶).



The doped crystals were calculated using 40-atoms supercells, which were eight times larger than the elementary cubic cell (four atoms) and twice larger than the elementary orthorhombic cell (20 atoms). The uniform k-mesh of 4x4x4 points in the Brillouin zone was used for the supercells, and twice larger grid for the pure compounds.

View Article Online
DOI: 10.1059/D0MA00452A

Acknowledgements

This research was supported by the Israel science foundation grant No. 937/18 and 2552/17. Calculations were performed using the PL-GRID infrastructure (Prometheus computer and supported by the National Science Centre in Poland (grant 2019/33/B/ST8/02105).

References

- 1 C. R. Kagan, D. B. Mitzi and C. D. Dimitrakopoulos, *Science* (80-.), 1999, **286**, 945–947.
- 2 Y. Fu, H. Zhu, J. Chen, M. P. Hautzinger, X. Y. Zhu and S. Jin, *Nat. Rev. Mater.*, 2019, **4**, 169–188.
- 3 J. Shamsi, A. S. Urban, M. Imran, L. De Trizio and L. Manna, *Chem. Rev.*, 2019, **119**, 3296–3348.
- 4 W. J. Nimens, S. J. Lefave, L. Flannery, J. Ogle, D.-M. Smilgies, M. T. Kieber-Emmons and L. Whittaker-Brooks, *Angew. Chemie Int. Ed.*, 2019, **58**, 13912–13921.
- 5 G. E. Eperon, S. N. Habisreutinger, T. Leijtens, B. J. Bruijnaers, J. J. van Franeker, D. W. deQuilettes, S. Pathak, R. J. Sutton, G. Grancini, D. S. Ginger, R. A. J. Janssen, A. Petrozza and H. J. Snaith, *ACS Nano*, 2015, **9**, 9380–9393.
- 6 Q. Wang, B. Chen, Y. Liu, Y. Deng, Y. Bai, Q. Dong and J. Huang, *Energy Environ. Sci.*, 2017, **10**, 516–522.
- 7 X. Li, M. Ibrahim Dar, C. Yi, J. Luo, M. Tschumi, S. M. Zakeeruddin, M. K. Nazeeruddin, H. Han and M. Grätzel, *Nat. Chem.*, 2015, **7**, 703–711.
- 8 G. Abdelmageed, L. Jewell, K. Hellier, L. Seymour, B. Luo, F. Bridges, J. Z. Zhang and S. Carter, *Appl. Phys. Lett.*, , DOI:10.1063/1.4967840.
- 9 N. Chander, A. F. Khan, P. S. Chandrasekhar, E. Thouti, S. K. Swami, V. Dutta and V. K. Komarala, *Appl. Phys. Lett.*, , DOI:10.1063/1.4891181.
- 10 F. Yang, D. Hirovani, G. Kapil, M. A. Kamarudin, C. H. Ng, Y. Zhang, Q. Shen and S. Hayase, *Angew. Chemie*, 2018, **130**, 12927–12931.



- 11 S. Xiang, W. Li, Y. Wei, J. Liu, H. Liu, L. Zhu and H. Chen, *Nanoscale*, 2018, **10**, 9996–10004. View Article Online
DOI: 10.1039/D0MA00452A
- 12 Y. Liang, L. Guan, X. Xu, S. Han, J. Guo, J. Wang, X. Chen, Z. Zhang and X. Li, *J. Phys. Chem. C*, 2020, **124**, 6028–6037.
- 13 A. Swarnkar, W. J. Mir and A. Nag, *ACS Energy Lett.*, 2018, **3**, 286–289.
- 14 Y. Wu, F. Xie, H. Chen, X. Yang, H. Su, M. Cai, Z. Zhou, T. Noda and L. Han, *Adv. Mater.*, 2017, **29**, 1701073.
- 15 K. Pinsuwan, C. Boonthum, T. Supasai, S. Sahasithiwat, P. Kumnorkaew and P. Kanjanaboos, *J. Mater. Sci.*, 2020, **55**, 3484–3494.
- 16 E. V. Péan, C. S. De Castro and M. L. Davies, *Mater. Lett.*, 2019, **243**, 191–194.
- 17 D. A. Gidlow, *Occup. Med. (Chic. Ill.)*, 2004, **54**, 76–81.
- 18 G. Flora, D. Gupta and A. Tiwari, *Interdiscip. Toxicol.*, 2012, **5**, 47–58.
- 19 R. A. Goyer, *Environ. Health Perspect.*, 1993, **100**, 177–187.
- 20 F. Li and M. Liu, *J. Mater. Chem. A*, 2017, **5**, 15447–15459.
- 21 G. E. Eperon, G. M. Paternò, R. J. Sutton, A. Zampetti, A. A. Haghighirad, F. Cacialli and H. J. Snaith, *J. Mater. Chem. A*, 2015, **3**, 19688–19695.
- 22 J. K. Nam, S. U. Chai, W. Cha, Y. J. Choi, W. Kim, M. S. Jung, J. Kwon, D. Kim and J. H. Park, *Nano Lett.*, 2017, **17**, 2028–2033.
- 23 M. Saliba, T. Matsui, J.-Y. Seo, K. Domanski, J.-P. Correa-Baena, M. K. Nazeeruddin, S. M. Zakeeruddin, W. Tress, A. Abate, A. Hagfeldt and M. Grätzel, *Energy Environ. Sci.*, 2016, **9**, 1989–1997.
- 24 C. Liu, W. Li, H. Li, H. Wang, C. Zhang, Y. Yang, X. Gao, Q. Xue, H.-L. Yip, J. Fan, R. E. I. Schropp and Y. Mai, *Adv. Energy Mater.*, 2019, **9**, 1803572.
- 25 W. Xiang, Z. Wang, D. J. Kubicki, W. Tress, J. Luo, D. Prochowicz, S. Akin, L. Emsley, J. Zhou, G. Dietler, M. Grätzel and A. Hagfeldt, *Joule*, 2019, **3**, 205–214.
- 26 T. Zhang, M. I. Dar, G. Li, F. Xu, N. Guo, M. Grätzel and Y. Zhao, *Sci. Adv.*, 2017, **3**, e1700841.
- 27 A. Marronnier, G. Roma, S. Boyer-Richard, L. Pedesseau, J.-M. Jancu, Y. Bonnassieux, C. Katan, C. C. Stoumpos, M. G. Kanatzidis and J. Even, *ACS Nano*, 2018, **12**, 3477–3486.
- 28 A. Shpatz Dayan, B.-E. Cohen, S. Aharon, C. Tenailleau, M. Wierzbowska and L. Etgar, *Chem. Mater.*, 2018, **30**, 8017–8024.



- 29 F. O. Saouma, C. C. Stoumpos, J. Wong, M. G. Kanatzidis and J. I. Jang, *Chem. Mater.*, 2018, **30**, 6668–6674. DOI:10.1038/s41467-017-00788-x. View Article Online
DOI:10.1039/D0MA00452A
- 30 A. K. Jena, A. Kulkarni, Y. Sanehira, M. Ikegami and T. Miyasaka, *Chem. Mater.*, 2018, **30**, 6668–6674.
- 31 H. Zhao, J. Xu, S. Zhou, Z. Li, B. Zhang, X. Xia, X. Liu, S. Dai and J. Yao, *Adv. Funct. Mater.*, 2019, **29**, 1808986.
- 32 T. Fujihara, S. Terakawa, T. Matsushima, C. Qin, M. Yahiro and C. Adachi, *J. Mater. Chem. C*, 2017, **5**, 1121–1127.
- 33 W. Ke, C. C. Stoumpos, I. Spanopoulos, L. Mao, M. Chen, M. R. Wasielewski and M. G. Kanatzidis, *J. Am. Chem. Soc.*, 2017, **139**, 14800–14806.
- 34 G. C. Papavassiliou and I. B. Koutselas, *Synth. Met.*, 1995, **71**, 1713–1714.
- 35 C. C. Stoumpos, C. D. Malliakas and M. G. Kanatzidis, *Inorg. Chem.*, 2013, **52**, 9019–9038.
- 36 E. J. W. Whittaker and R. Muntus, *Geochim. Cosmochim. Acta*, 1970, **34**, 945–956.
- 37 G. Kieslich, S. Sun and A. K. Cheetham, *Chem. Sci.*, 2014, **5**, 4712–4715.
- 38 Z. Li, M. Yang, J. S. Park, S. H. Wei, J. J. Berry and K. Zhu, *Chem. Mater.*, 2016, **28**, 284–292.
- 39 M. Deepa, M. Salado, L. Calio, S. Kazim, S. M. Shivaprasad and S. Ahmad, *Phys. Chem. Chem. Phys.*, 2017, **19**, 4069–4077.
- 40 D. Sabba, H. K. Mulmudi, R. R. Prabhakar, T. Krishnamoorthy, T. Baikie, P. P. Boix, S. Mhaisalkar and N. Mathews, *J. Phys. Chem. C*, 2015, **119**, 1763–1767.
- 41 I. Chung, B. Lee, J. He, R. P. H. Chang and M. G. Kanatzidis, *Nature*, 2012, **485**, 486–489.
- 42 N. Wang, Y. Zhou, M.-G. Ju, H. F. Garces, T. Ding, S. Pang, X. C. Zeng, N. P. Padture and X. W. Sun, *Adv. Energy Mater.*, 2016, **6**, 1601130.
- 43 H. Xu, J. Duan, Y. Zhao, Z. Jiao, B. He and Q. Tang, *J. Power Sources*, 2018, **399**, 76–82.
- 44 B. Li, R. Long, Y. Xia and Q. Mi, *Angew. Chemie - Int. Ed.*, 2018, **57**, 13154–13158.
- 45 F. Reyes-Pérez, J. J. Gallardo, T. Aguilar, R. Alcántara, C. Fernández-Lorenzo and J. Navas, *ChemistrySelect*, 2018, **3**, 10226–10235.
- 46 S. Liu, L. Yuan, Y. Zhao, Y. Chen, W. Xiang and X. Liang, *J. Alloys Compd.*,



- 2019, **806**, 1022–1028.
- 47 J. Liang, P. Zhao, C. Wang, Y. Wang, Y. Hu, G. Zhu, L. Ma, J. Liu and Z. Jin, *J. Am. Chem. Soc.*, 2017, **139**, 14009–14012.
- 48 N. Li, Z. Zhu, J. Li, A. K.-Y. Jen and L. Wang, *Adv. Energy Mater.*, 2018, **8**, 1800525.
- 49 J. L. Knutson, J. D. Martin and D. B. Mitzi, *Inorg. Chem.*, 2005, **44**, 4699–4705.
- 50 A. Goyal, S. McKechnie, D. Pashov, W. Tumas, M. Van Schilfgaarde and V. Stevanović, *Chem. Mater.*, 2018, **30**, 3920–3928.
- 51 T. Leijtens, R. Prasanna, A. Gold-Parker, M. F. Toney and M. D. McGehee, *ACS Energy Lett.*, 2017, **2**, 2159–2165.
- 52 R. K. Misra, L. Ciammaruchi, S. Aharon, D. Mogilyansky, L. Etgar, I. Visoly-Fisher and E. A. Katz, *ChemSusChem*, 2016, **9**, 2572–2577.
- 53 M. Zhang, M. Ye, W. Wang, C. Ma, S. Wang, Q. Liu, T. Lian, J. Huang and Z. Lin, *Adv. Mater.*, 2020, **32**, 2000999.
- 54 X. D. Zhu, Y. Xie and Y. T. Liu, *J. Mater. Chem. A*, 2018, **6**, 21255–21260.
- 55 Y. Takahashi, H. Hasegawa, Y. Takahashi and T. Inabe, *J. Solid State Chem.*, 2013, **205**, 39–43.
- 56 C. Wehrenfennig, G. E. Eperon, M. B. Johnston, H. J. Snaith and L. M. Herz, *Adv. Mater.*, 2014, **26**, 1584–1589.
- 57 G. Xing, N. Mathews, S. Sun, S. S. Lim, Y. M. Lam, M. Gratzel, S. Mhaisalkar and T. C. Sum, *Science (80-.)*, 2013, **342**, 344–347.
- 58 A. Miyata, A. Mitioglu, P. Plochocka, O. Portugall, J. T. W. Wang, S. D. Stranks, H. J. Snaith and R. J. Nicholas, *Nat. Phys.*, 2015, **11**, 582–587.
- 59 L. Ji, X. Zhang, T. Zhang, Y. Wang, F. Wang, Z. Zhong, Z. D. Chen, Z. Xiao, L. Chen and S. Li, *J. Mater. Chem. A*, 2019, **7**, 9154–9162.
- 60 F. Hao, C. C. Stoumpos, D. H. Cao, R. P. H. Chang and M. G. Kanatzidis, *Nat. Photonics*, 2014, **8**, 489–494.
- 61 V. K. Ravi, G. B. Markad and A. Nag, *ACS Energy Lett.*, 2016, **1**, 665–671.
- 62 C. Liu, M. Hu, X. Zhou, J. Wu, L. Zhang, W. Kong, X. Li, X. Zhao, S. Dai, B. Xu and C. Cheng, *NPG Asia Mater.*, 2018, **10**, 552–561.
- 63 Y. Hu, F. Bai, X. Liu, Q. Ji, X. Miao, T. Qiu and S. Zhang, *ACS Energy Lett.*, 2017, **2**, 2219–2227.
- 64 F. Haque, M. Wright, M. A. Mahmud, H. Yi, D. Wang, L. Duan, C. Xu, M. B.

View Article Online
DOI: 10.1039/D0MA00452A



- Upama and A. Uddin, *ACS Omega*, 2018, **3**, 11937–11944.
- 65 P. Giannozzi, S. Baroni, N. Bonini, M. Calandra, R. Car, C. Cavazzoni, D. Ceresoli, G. L. Chiarotti, M. Cococcioni, I. Dabo, A. Dal Corso, S. De Gironcoli, S. Fabris, G. Fratesi, R. Gebauer, U. Gerstmann, C. Gougoussis, A. Kokalj, M. Lazzeri, L. Martin-Samos, N. Marzari, F. Mauri, R. Mazzarello, S. Paolini, A. Pasquarello, L. Paulatto, C. Sbraccia, S. Scandolo, G. Sclauzero, A. P. Seitsonen, A. Smogunov, P. Umari and R. M. Wentzcovitch, *J. Phys. Condens. Matter*, , DOI:10.1088/0953-8984/21/39/395502.
- 66 M. Wierzbowska, J. J. Meléndez and D. Varsano, *Comput. Mater. Sci.*, 2018, **142**, 361–371.

View Article Online
DOI: 10.1039/D0MA00452A



